SPE-215661-MS

Thermal Fracturing Simulation for Flow Assurance in CCS

Jason Park, Cas Berentsen, and C. J. Hans de Pater, Fenix Consulting Delft

This paper was prepared for presentation at the SPE International Hydraulic Fracturing Technology Conference and Exhibition held in Muscat, Sultanate of Oman, 12 - 14 September 2023.

Abstract

CO2 injection into depleted gas fields causes long-term cooling of the reservoir. Therefore, even if injection pressure stays below the fracture initiation pressure, the cooled volume still creates an extensive stress disturbance that can induce propagation of large fractures over time. The enhanced injectivity after the onset of this thermal fracturing might jeopardize injection operations due to the risk of hydrate plugging in the injection well caused by the combination of low pressure and low temperature, and large fractures may also increase the risk of loss of containment. Modeling the fracture evolution provides an estimate of these effects and their timing.

Coupled simulation of CO2 injection provides the thermal fracture dimensions for a given uncertainty in the reservoir parameters. Simplified stress modelling is applied in the thermal fracture reservoir simulation, but a full 3D geomechanical model that was developed for fault slip analysis provides accurate estimates of the stress state after depletion and the subsequent evolution of the stresses during CO2 injection. For computation efficiency, sector models were used with locally refined grids to accommodate fractures in the reservoir simulation model. It was verified that the fracture models match the full-field simulation under matrix flow conditions. The fracture simulations were developed in close relation with flow assurance modeling to determine the operational windows that avoid hydrate formation while maintaining the required injection target.

Thermal fracture propagation by CO2 injection into the depleted Dutch offshore gas field has been simulated by using coupled simulation approach. The model has been developed with geomechanical properties and stresses obtained from various sources in neighboring fields. It was found that stress, thermal expansion coefficient, modulus and permeability distribution are the principal parameters that determine fracture growth. The forecast of thermal fracture propagation yielded in some cases very long fractures reaching compartment boundaries. Injectivity was enhanced by up to a factor of 4, which is significant for flow assurance. The coupled modeling of thermal fracturing provides mitigating measures in case the temperature and pressure drop into the hydrate formation window.

Introduction

PORTHOS (Port Of Rotterdam CO2 Transport Hub and Offshore Storage) is a project to transport and store CO2 in the depleted offshore P18 gas field in the Netherlands. The process involves several steps. First, the CO2 emissions will be captured from industrial sources in the Rotterdam port area. Once captured, the CO2 will be transported through a collective pipeline system. To prepare the CO2 for storage, it will be pressurized using a compressor station. After pressurization, the CO2 will be injected into the depleted P18 gas field, which is no longer being used for natural gas production (Figure 1). The overall goal of the PORTHOS project is to store a total of 37 million tons of CO2 over a period of 15 years. The annual injection target is set at 2.5 million tons of CO2. The total planned CO2 storage will be 37 million tons with annual injection target of 2.5 million tons for 15 years (www.porthosco2.nl/en/project/, 2023).

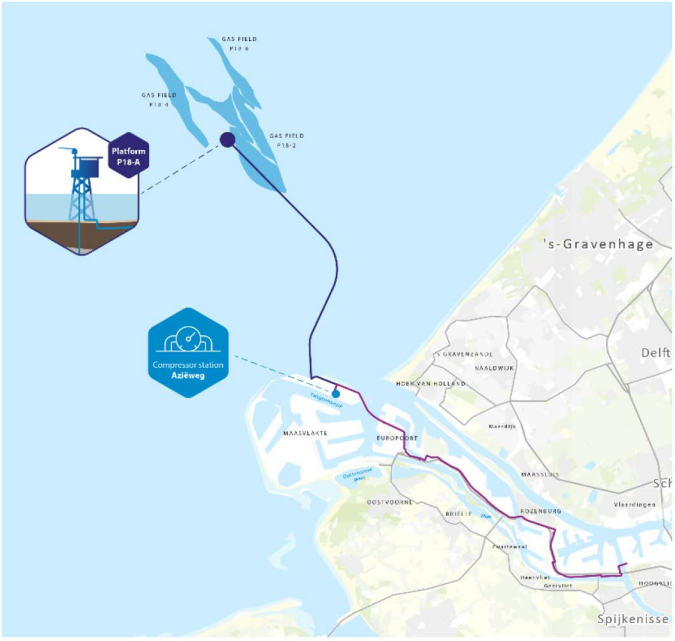

Figure 1—Overview of PORSHOS CO2 transport and storage project. It is located approximately 20 km away from the Rotterdam harbor (https://www.porthosco2.nl/en/project/).

The P18 cluster consists of three fields: the P18-2, P18-4 and P18-6 and they are located approximately at 3,500 m below the sea floor. The P18-2 and P18-4 fields are planned for CO2 storage but the P18-6 is considered as a back-up storage due to relative lower injectivity and the limited storage capacity compared to P18-2 and P18-4. The locations of fields in the P18 cluster is shown in Figure 2. As shown in the figure, P18-2 field consists of 4 compartments and there is only one compartment in P18-4 field. Gas production started in 1993 and the peak annual production of 2.2 Bcm reached in 1998. The total cumulative gas production in P18 cluster was 13.5 Bcm at the end of June 2018 (Neele et al., 2019).

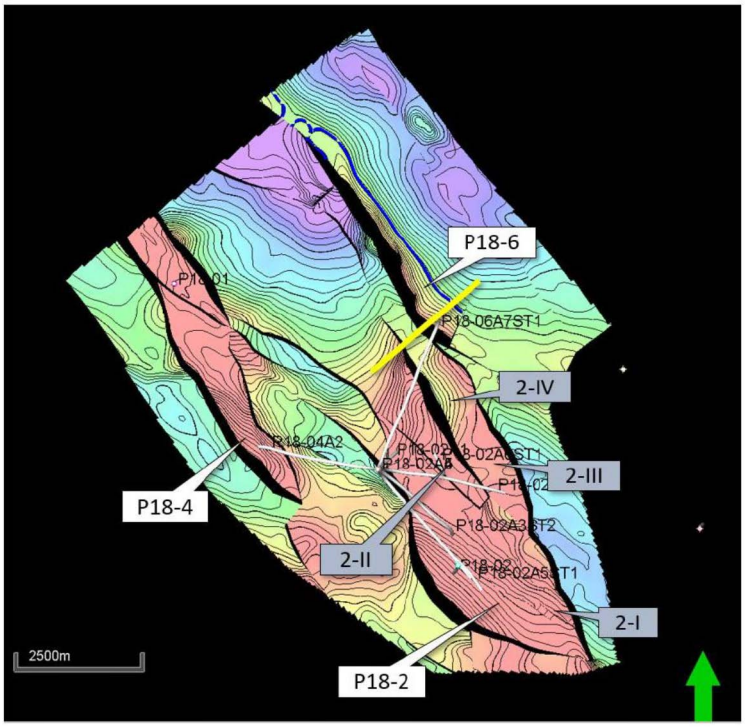

Figure 2—3D view of the top Bunter in the P18-02, P18-04 and P18-06 fields (Neele et al., 2019).

The reservoir rocks of the P18 gas fields belong to the Lower Germanic Trias Group, which is informally called Bunter. The subgroups in Bunter are the Hardegsen, Upper and Lower Detfurth and Volpriehausen formations as shown in Figure 3. The youngest Hardegsen formation has the biggest *kh* contributions, 70-90% of total *kh*, in the historical wells (Table 1). The tight Volpriehausen formation has only a small contribution to the total CO2 storage capacity. The permeability distribution shows quite big heterogeneity. Even in the Hardegsen formation, the effective permeabilities in P18-2A1 well are in the ranges of 1-80 mD and they are in the ranges of 100-500 mD in P18-2A5 well. The seals of the P18 reservoir are the Upper Germanic Trias Group and the Jurassic Altena Group. The Upper Germanic Trias Group is approximately 155 m thick in P18-2 field and directly above this lies the thick Altena Group which is approximately 500 m thick. The total thicknesses of the caprock in P18 are in the range between 450 m and 750 m. As the gas column of nearly 600 m could be maintained in P18-2 field, the seal capacity is excellent (Neele et al., 2019).

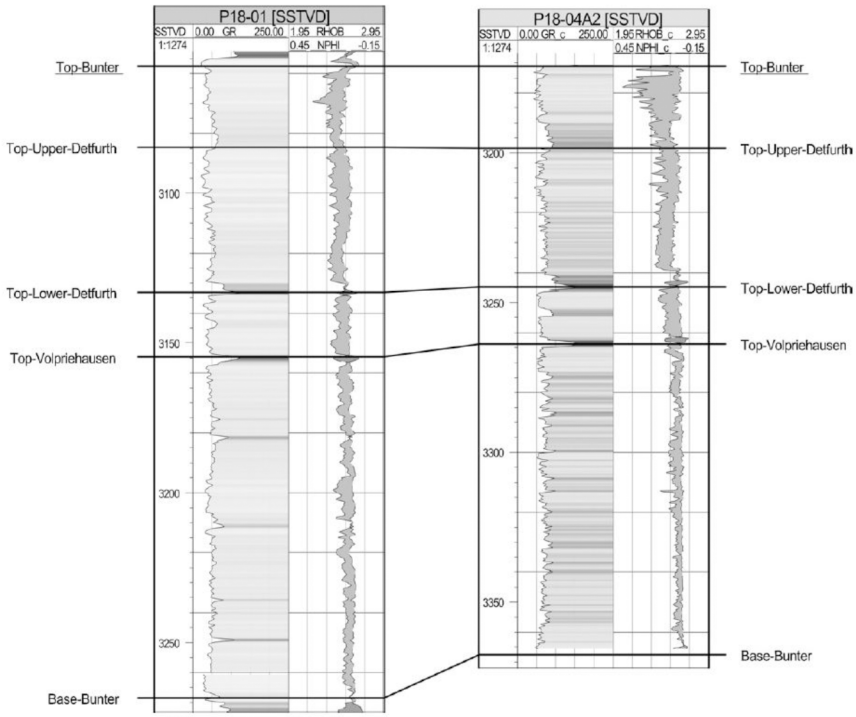

Figure 3—Reservoir rocks in P18 fields (Arts et al., 2012).

Table 1—Effective *kh* and porosity of reservoir rocks in production wells in P18 fields.

Property	*kh* (mD-m)		Porosity (%)		Average Thickness (m)
Well	P18-4A2	P18-2A5	P18-4A2	P18-2A5	
Hardegsen	3,750	8,530	0.15	0.15	20
Detfurth + Volpriehausen	345	4445	0.06	0.09	165

Flow assurance study provides safe operational windows for CO2 injection in the reservoir by avoiding, for example, two phase flow in pipelines, slug flow in the tubing and hydrate formation in the reservoir, etc. The study generates valuable outcomes such as the ranges of pipeline and tubing diameters, different injection rates and temperatures per different reservoir pressures, and shut-in and start-up strategies. Figure 4 illustrates the iterative loop encompassing flow assurance, reservoir simulation, and geomechanics. For a certain set of operational conditions, flow assurance modeling provides CO2 injection rates and temperatures. These are used in the thermal fracture simulation to compute the resulting thermal fracture growth and pressure response that are fed back to flow assurance to update their injection scheme. Additionally, the pressure and temperature distribution derived from the thermal fracture simulation serve as inputs for fault stability analysis, which is performed using a geomechanical model. Following this, an optimization step is executed to update the well injectivity and accommodate geomechanical constraints. If necessary, further iterations can be performed to refine the results.

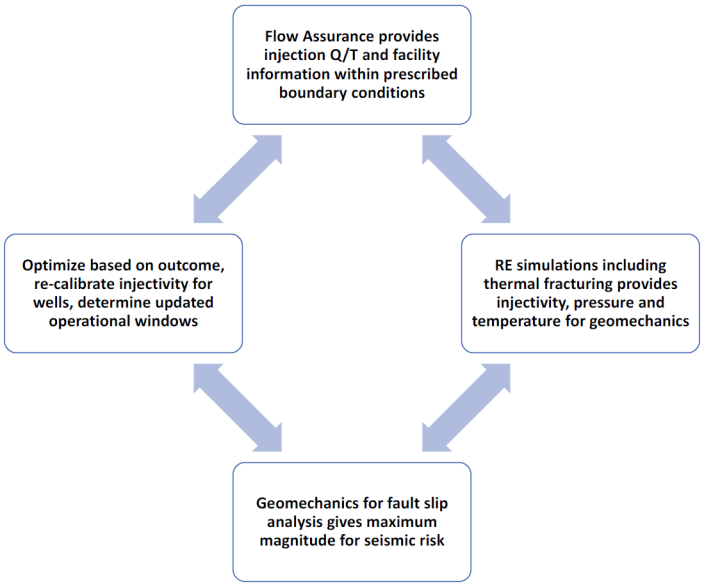

Figure 4—CCS iteration loop from flow assurance, coupled reservoir simulation and geomechanics (de Pater et al., 2021).

The injection of low temperature CO2 will cool the reservoir, resulting in induced thermal fracturing near the wellbore. Thermal fracture will increase the injectivity which may result in higher Joule-Thomson cooling in the near-wellbore region causing hydrate plugging in the well or reservoir. Thermal fractures might also penetrate the cap rock and could jeopardize the integrity of the cap rock. If the thermal fracture propagates towards a fault, the cold front reaches the fault and it could induce fault slippage as well. The possible extreme geomechanical limitations in the reservoir were evaluated in the original study (de Pater et al., 2021) by taking following possible extreme scenarios:

- The geomechanical parameters were selected such that plausible cases with the most extreme fracture growth and highest risk for fault stability have been covered
- In order to investigate the maximum possible thermal stress reduction, a scenario with high injection rate without maximum injection bottom-hole pressure limit has been simulated
- The well closest to the fault was chosen as the main injector in order to investigate the maximum effect on the fault instability

In this paper, the effects of thermal stress reduction by CO2 injection have been evaluated in the P18-2 and P18-4 fields in terms of the thermal fracture propagation. Based on the history matched reservoir simulation model, enhanced coupled thermal fracture models have been developed by adding geomechanical properties from log and core analysis, which account for a wider range to include possible worst case scenarios. The initiation of thermal fracture has been investigated in terms of temperature and stress conditions near the well. The possible effects on flow assurance by the increase of injectivity by thermal fracturing has also been investigated. The effects of high permeability layers on thermal fracture propagation has been discussed at the end of the paper.

Thermal Fracture Simulation Model Building

The history matched reservoir simulation model for P18-2 field is shown in Figure 5. Because the North part of the field did not contribute during the production due to the poor reservoir quality, only the South part of the field will be used for CO2 storage. The current plan is to use locations of the historical production wells as the locations for the future injection wells, which are shown in the figure. Depleted pressure after natural gas production in the Hardegsen and Upper Detfurth formations along the wells is approximately 2,000 kPa, and it is 4,000-6,000 kPa in the Volpriehausen formation. The depletion is 33,000 kPa in the Hardegsen

and the Upper Detfurth compared to the initial pressure of 35,000 kPa. The permeability is the highest in the Hardegsen formation and there are a few high permeability streaks with the effective permeabilities as high as 500-1,000 mD. However, the permeabilities in the Hardegsen formation near P18-2A1 well are relatively lower compared to the other regions and they are in the range of 1-50 mD. The permeabilities in the Volpriehausen formation are in the range of 0.1-5 mD.

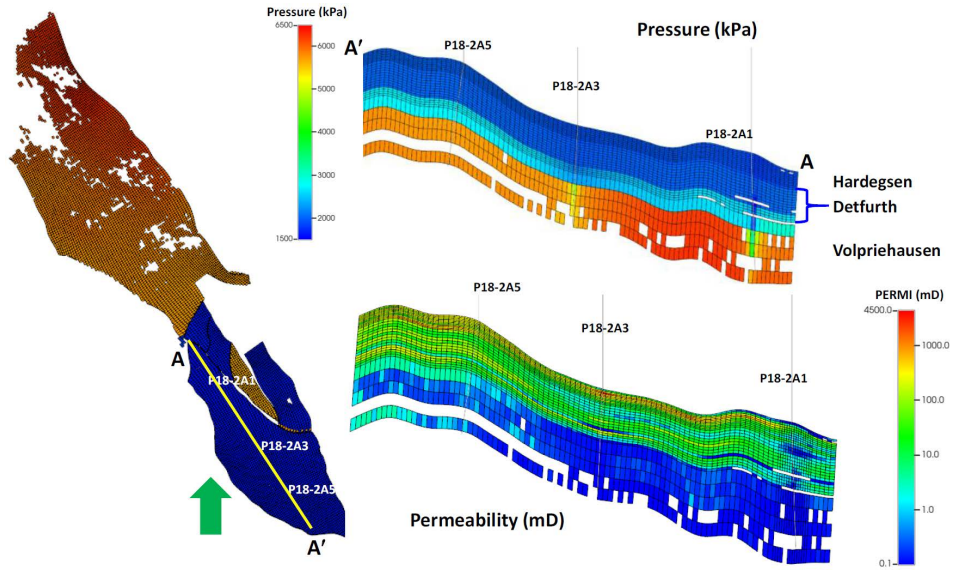

Figure 5—P18-2 history matched model. Left: top view of the model (pressure), right-top: cross-sectional view of pressure along the wells (A-A′) and right-bottom: cross-sectional view of effective permeability along the wells.

Host Grid Refinement in the Sector Models

Starting from the history matched models for the P18-2 and P18-4 fields, enhanced models have been built to simulate thermal fracture propagation (Figure 6). Compared to Figure 5, all the non-essential parts in P18-2 field which do not contribute to CO2 storage capacity have been de-activated in the sector models. As the P18-2 and P18-4 fields are separated by bounding faults, two different sector models have been made. In P18-2 three CO2 injection wells and in P18-4 one well have been planned.

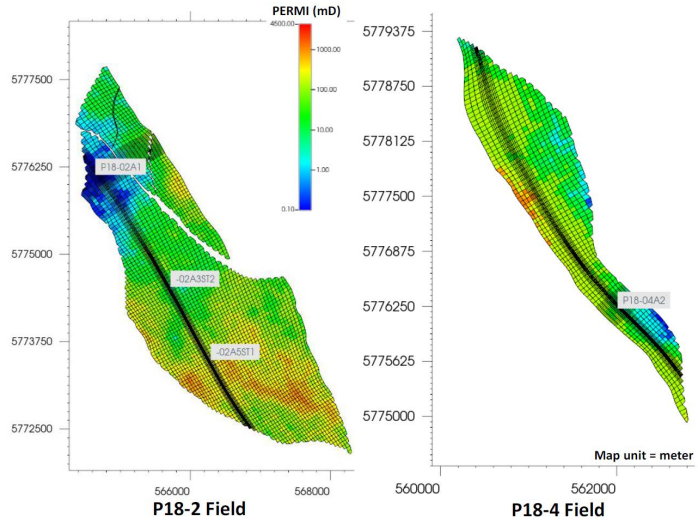

Figure 6—Two separate sector models for P18-2 and P18-4 fields have been made.

In order to capture the detailed geomechanical changes over the injection period in the near wellbore region two different grid refinements have been made depending on thermal fracture directions as shown in Figure 7. For the longitudinal fracture model, the width of most refined cells is 10 m and the width of less refined cells is 15 m. The same refinement has been applied to the j-direction in the transverse fracture model.

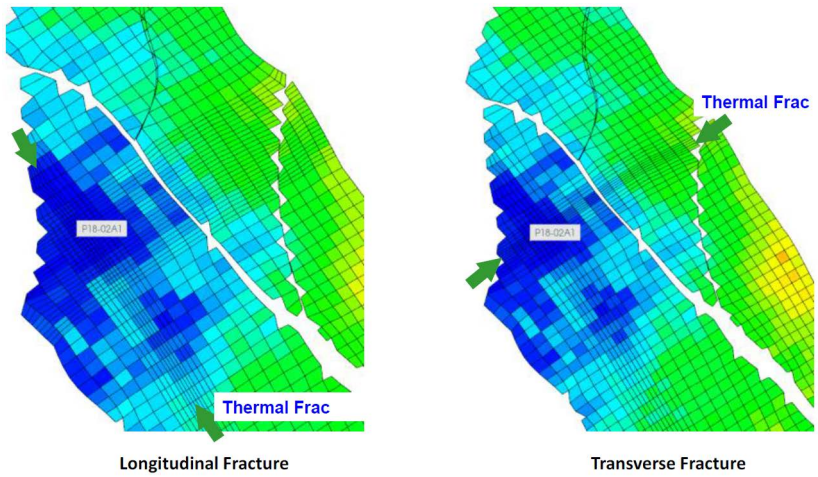

Figure 7—Host grid refinements for the longitudinal fracture and for the transverse fracture around P18-2A1 well. The green arrows indicate the i-direction in the left figure and j-direction in the right figure

Geomechanical Properties. Geomechanical properties have been derived from core tests, log analysis and minifracs and they are summarized in Table 2. This resulted in a Young's modulus of 27 GPa and a Poisson ratio of 0.2 in the reservoir formations. The vertical stress are estimated from the density log. The range for minimum horizontal stress was estimated from the leak-off-test data and fracture treatments data in the nearby fields. The maximum horizontal stress is estimated from regional drilling data. Because the stress is quite uncertain the stress data in the model was taken much conservatively. Stress orientation is assumed to be the same as the regional stress direction, which is 40°NW in the maximum stress direction. The details of methods to derive the geomechanical data is discussed in the original study (de Pater et al., 2021).

Table 2—Average geomechanical properties, including the ranges used for the simulation and the estimated uncertainty range. The parameters are ranked by importance for the outcome of the simulations.

Parameter (Hierarchy by Effects)	Unit	Base Case	Simulated Range	Uncertainty Range	Comments
Min. Hor. Stress Gradient (Virgin)	(kPa/m)	14.5	14.0-14.5	14.0-16.0	Nearby minifracs
Biot coefficient	(-)	0.8	0.8-1.0	0.6-0.9	Derived from Young's modulus, Poisson ratio and grain modulus
Young's modulus	(GPa)	27	27	18-36	Measured
Linear Thermal expansion Coef.	(1/K)	9.0E-06	9.0E-06	low	Measured
Poisson ratio	(-)	0.20	0.15-0.20	0.15-0.25	Measured
Initial Reservoir Pressure	(bar)	[348, 375]	[348, 375]	low	Measured
Initial Reservoir Temperature	(°C)	[117, 126]	[117, 126]	low	Measured

Parameter (Hierarchy by Effects)	Unit	Base Case	Simulated Range	Uncertainty Range	Comments
Depleted Reservoir Pressure	(kPa)	2000	2000	low	Measured
Vertical Stress Gradient (Virgin)	(kPa/m)	20.5	20.5	low	Density log
Max. Hor. Stress Gradient (Virgin)	(kPa/m)	16	16	15-19	Regional data
Rock Heat Capacity	(J/kg·K)	1000.0	1000.0	low	Measured
Rock Thermal Conductivity	(J/m·s·K)	2.0	2.0	intermediate	Measured

In the original study a wide range of sensitivities have been investigated. In this paper only the "worst" case scenario will be discussed. This assumes the lower end of the stress gradient of 14.0 kPa/m, a Poisson's ratio of 0.15 and a high Biot coefficient of 1.0. This gives the most favorable conditions for thermal fracture propagation and it is the worst possible scenario in the perspective of flow assurance.

Barton-Bandis Model. The thermal fracture simulation in the software is facilitated by a smeared crack approach using Barton-Bandis fracture model. This model is based on a dual-permeability formulation in a reservoir consisting of natural fractures and matrix (CMG, 2022). In this model, a fracture is simulated as an increased permeability in the fracture domain instead of explicitly simulating the induced fracture with width, height and length. The fracturing criterion used in the software is based on effective stress, which is appropriate because thermal fractures are not induced by high fluid pressure cracking the rock but by tensile strain induced by effective stress change resulting pre-dominantly from cooling. If the effective tensile stress falls below a tensile strength then the fracture starts to propagate.

A schematic relationship for the fracture permeability as a function of stress is shown in Figure 8. If the stress in the cell is less than the fracture opening stress (σ_{fo}), the fracture opens and the permeability in the cell increases to the pre-set fracture permeability of 10 Darcy. The followings are descriptions of the Barton-Bandis model in Figure 8:

- Path AB: stress in the fracture blocks > fracture open stress, fracture permeability = the same as initial model matrix perm (k_{matrix})
- Path BC: stress in the fracture blocks ≤ fracture open stress (= - 2,000 kPa), the fracture initiates and fracture permeability increases to k_f (= 10,000 mD) immediately
- Path DCE: as long as stress is less than zero, fracture permeability remains k_f
- Path EF: when the stress turn compressive again the fracture permeability reduces instantaneously to fracture closure permeability k_{cf} (= 200 mD) as the fracture does not immediately close completely
- Path FG: for increasing compressive effective stress, the permeability decreases asymptotically to the matrix permeability

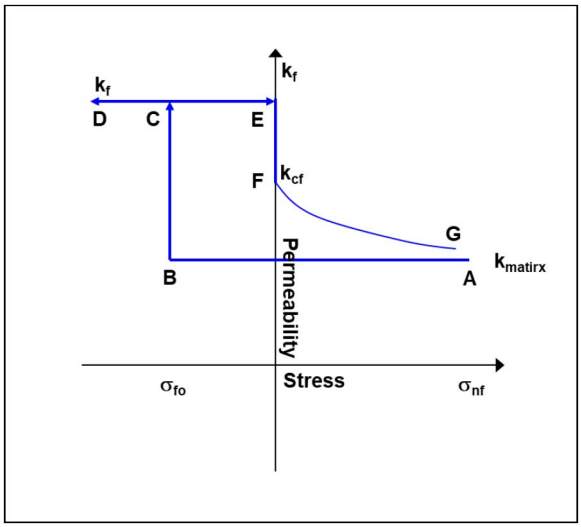

Figure 8—Schematic diagram for the Barton-Bandis model.

Thermal Fracture Simulation Results

Initiation of Thermal Fracture

For the worst case injection scenario, Figure 9 shows the CO2 injection rate and injection bottomhole temperature for the P18-2A1 well. The average rate is 1.7×10^6 sm^3/d and the total injection volume is 6.7×10^9 sm^3 (13 million tons) over 10 years of injection. Bottomhole injection temperature varies between 59 and 78°C except for the initial one month of high temperature injection period (91°C). This scenario is regarded as the "worst" due to the higher injection rate during a short injection duration compared to other scenarios.

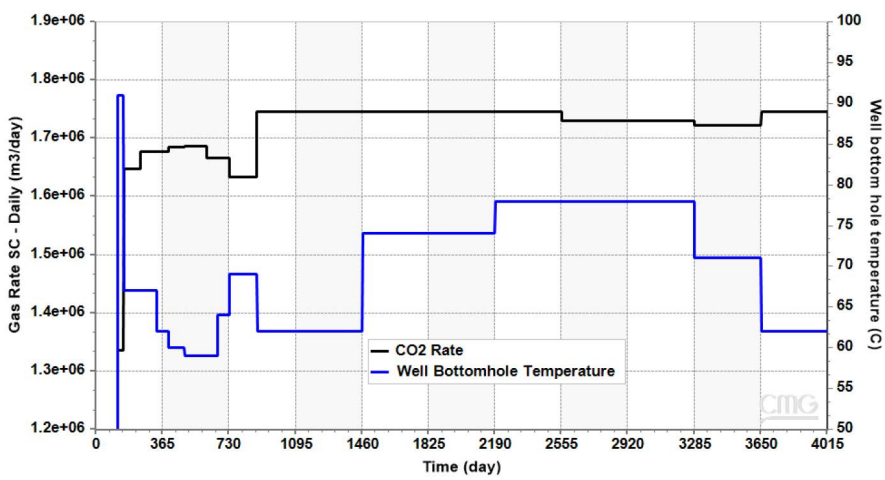

Figure 9—The worst case injection scenario in P18-2A1 well.

The near wellbore cross-section along the possible thermal fracture plane is presented in Figure 10 with temperature, minimum effective principal stress and a possible thermal fracture propagation after 2 months of injection. A thermal fracture initiates in three cells in the Hardegsen formation, resulting from thermal stress reduction by the cold CO2 injection. Figure 11 shows the temperature, pressure and saturation in the reservoir as function of the distance from the wellbore along the A-A′ path that aligns with the fracture plane. As shown the temperature within the reservoir falls below the CO2 injection temperature of 67°C. This drop in temperature results from Joule-Thomson effect and water vaporization. During the simulation the maximum additional cooling on top of the injection temperature reached 18°C.

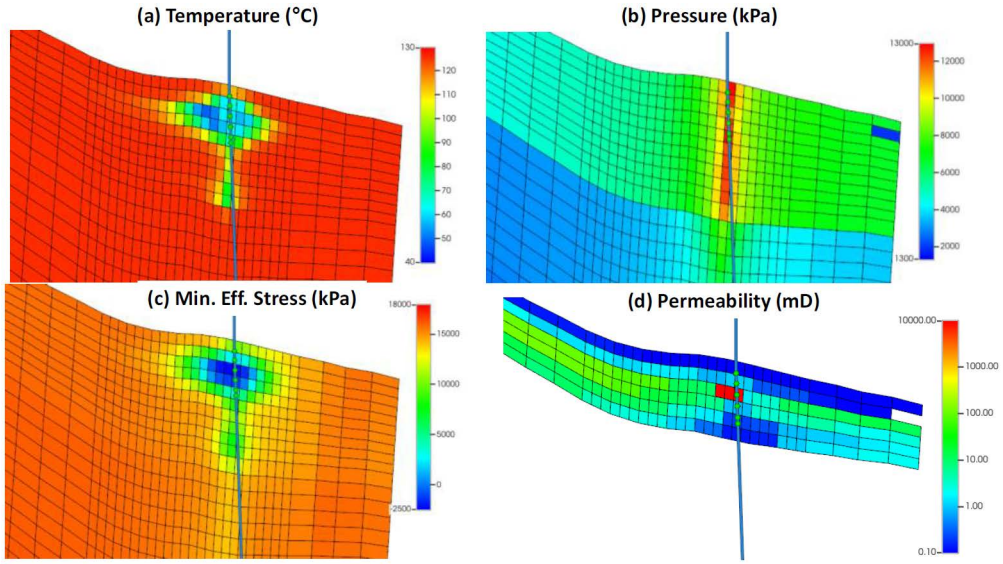

Figure 10—The initiation of thermal fracture in P18-2A1 well after injecting CO2 for 2 months. Thermal fracture is shown as high permeability cells (10 Darcy) in the model.

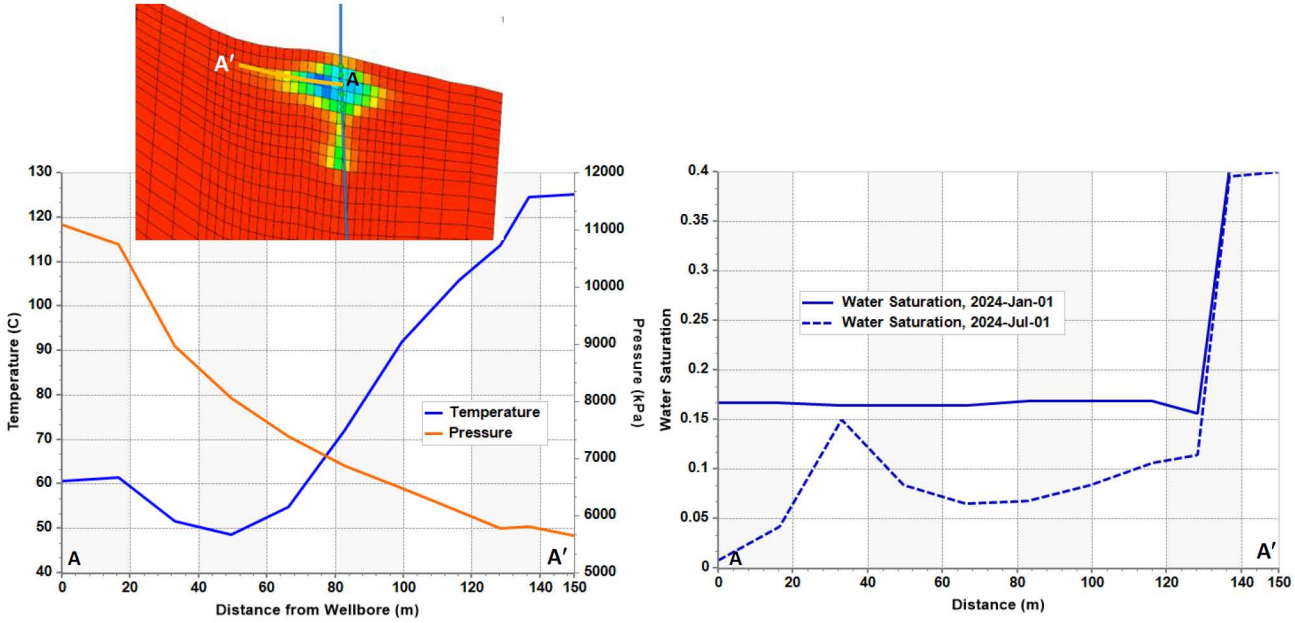

Figure 11—Temperature change (left) and water saturation change from wellbore into reservoir (A-A′) due to CO2 injection at 2 months injection.

Because the Joule-Thomson coefficient of pure CO2 is inversely proportional to pressure at the injection temperature of 50-80°C (Creusen, 2018), the temperature in the vicinity of the wellbore (< 20 m), where the pressure is higher resulting in less Joule-Thomson cooling, is higher than the temperature away from the wellbore (30-70 m). On top of this effect there could be residual heat during the initial high temperature injection (90°C) in the near wellbore region. Due to the residual heat provided by the reservoir grains, the cooling effect diminishes as the distance is getting away from the wellbore (> 70 m). Initial water saturation of 17% has also decreased by vaporization to almost 0% near wellbore and to 7% around 60-100 m away from the well depending on the permeability.

The change of minimum effective stress in one of the cell where the thermal fracture initiates during two months is shown in Figure 12. The stress reduction in the simulation model is 18,160 kPa, and it is close

to the value of 18,582 kPa which is derived from the theoretical thermal stress reduction calculated with following equation (Fjær et al., 2008):

$$\Delta\sigma_T = \frac{\alpha_T E}{1-\nu}\Delta T$$

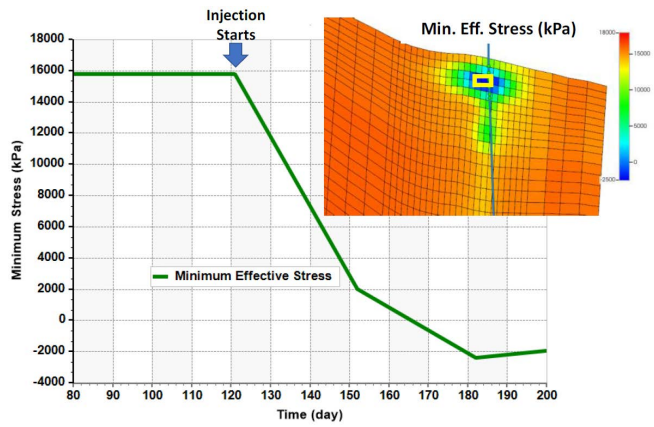

Figure 12—The change of minimum effective stress in the cell where the thermal fracture propagates.

where, α_T is the thermal expansion coefficient (9.0E-6 1/K), E is the Young's modulus (27 GPa), ν is the Poisson ratio (0.15) and ΔT is the temperature difference (65 deg C).

Fracture Propagation and Temperature Distribution

Thermal fracture propagations and temperature distributions over several time steps are shown in Figure 13. First of all, thermal fracture propagation follows the cold temperature front, and at the end of the injection the thermal fracture reaches one of the nearby faults with a total length of approximately 1000 m. Figure 14 compares the temperature distributions near P18-2A1 well at the end of CO2 injection between the thermal fracture model and matrix injection model. Due to the high fracture conductivity, the temperature distribution is a lot more elongated and narrower in the thermal fracture model along the maximum stress direction than the matrix injection model.

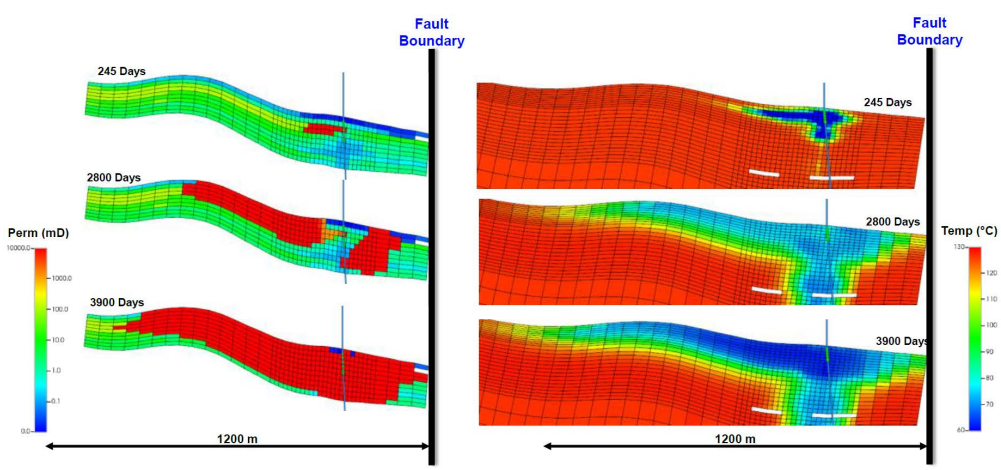

Figure 13—Thermal fracture propagations and temperature distributions over injection time. Please be noted that the fracture is presented in the fracture domain and the temperature is presented in the matrix domain.

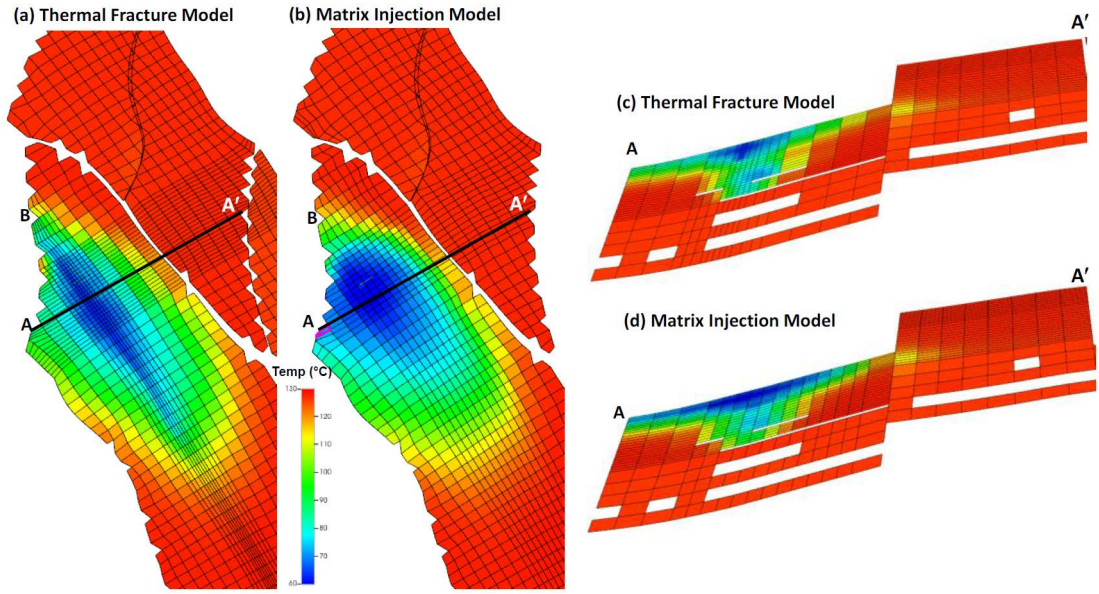

Figure 14—Temperature distribution comparisons between thermal fracture case (a and c) and matrix injection case (b and d). Top view of one of the Hardegsen layers (a and b in layer #3) and cross-section alone A-A′ in (c) and (d).

Figure 15 compares the temperature evolution at two different locations "A" and "B" on one of the faults as indicated in Figure 14. As the location "A" is further away from the thermal fracture, less CO2 flows toward this location in the thermal fracture model. However in the matrix model the high matrix permeability around the well (Figure 16) facilitates the CO2 flow toward location "A", causing temperature at this location to be lower compared to the fracture model. On the other hand, as the location "B" is in direct contact with the thermal fracture, the temperature in the fracture model at location "B" is lower than in the matrix model. The maximum temperature difference is 30°C at the location "A" and it is 15°C at the location "B" between the thermal fracture model and the matrix model. These differences in the temperature distribution might have considerable consequences for the stability of such faults.

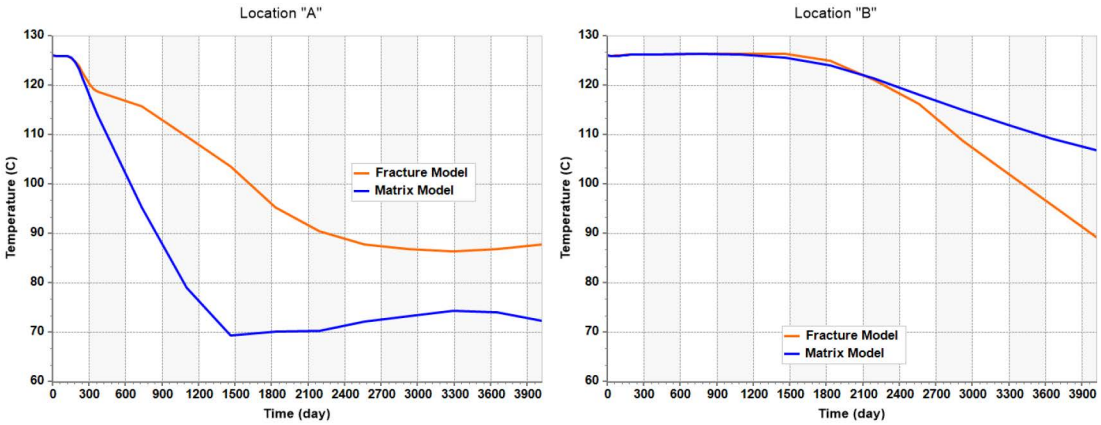

Figure 15—Comparison of the temperature change between the fracture and matrix model at locations "A" and "B" as shown in Figure 14.

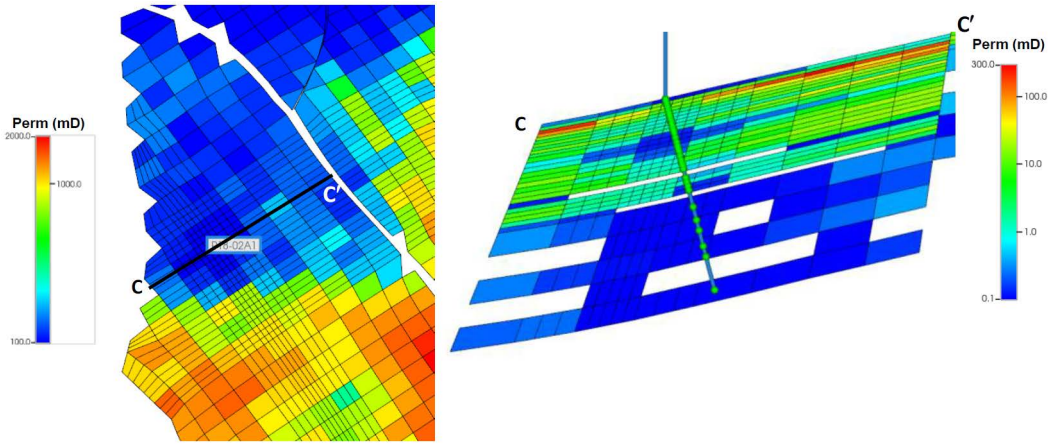

Figure 16—Matrix permeability distribution in one of the Hardegsen layers (layer #3, left) and cross-section alone C-C′ (right). Please be noted that the scale difference between two figures.

Injectivity Comparison

The injectivity improvement by thermal fracture propagation is shown in terms of injection bottomhole pressure in Figure 17. The maximum injection BHP difference between thermal fracture and matrix injection models is 26,000 kPa. The excess pressure is defined as the difference between the injection BHP and the average reservoir pressure in near wellbore region. The excess pressure in the fracture model is approximately a factor 4 lower than in the matrix model.

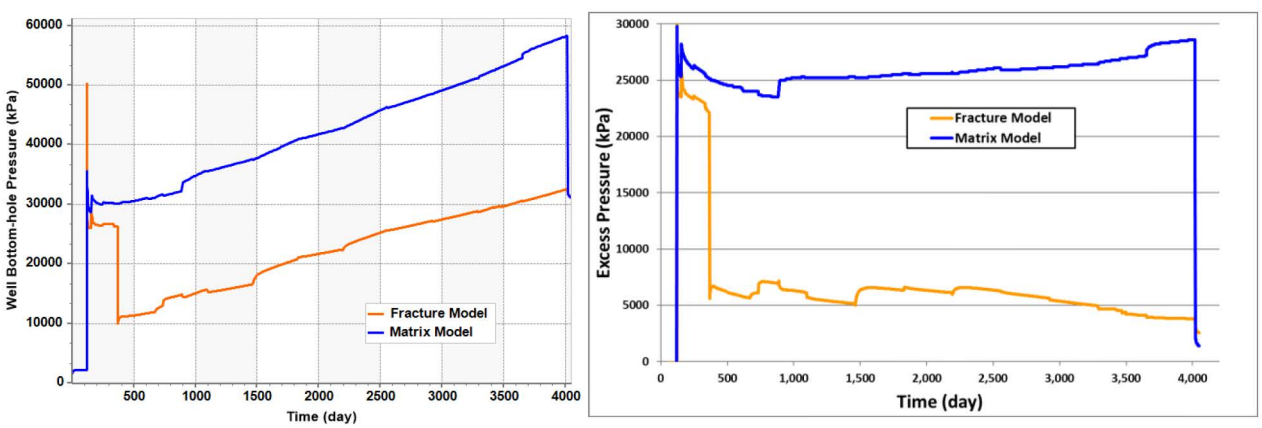

Figure 17—Bottomhole pressure and excess pressure comparisons between the matrix model and the fracture model in P18-2A1 well.

Figure 18 illustrates the potential impact of reducing the excess pressure on injection condition changes, considering only the basic phase behaviors and not accounting for any flow assurance aspects. It shows that the injection conditions have changed from a stable supercritical region for matrix injection (blue) towards a condition that is close to the gas phase injection (orange) when the thermal fracture is taken into account. This highlights the necessity for a comprehensive examination of flow assurance when estimating the potential decrease in injection bottomhole pressure caused by thermal fracturing.

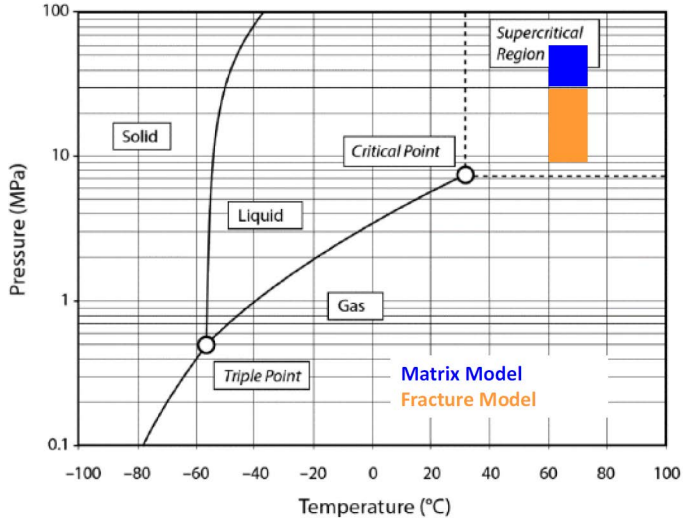

Figure 18—A simple example of estimation of the injection conditions change with injection bottomhole pressure change. The rectangles represent the overall operational ranges regarding temperature and BHP. For example in the fracture model, the injection pressure is in the range of 9,000-30,000 kPa and the injection temperature is in the range of 59-78 deg C. Phase diagram is taken from Nordbotten and Celia (2012).

Effect of permeability on thermal fracture propagation

Permeability distributions near the P18-2A3 and P18-2A5 wells are shown in Figure 19. The effective permeabilities in reservoir horizons are compared in Table 3. The table shows that the permeabilities in the Hardegsen, Detfurth and Volpriehausen formations are all much higher in around the P18-2A3 and P18-2A5 wells compared to surroundings of the P18-2A1 well (Figure 16).

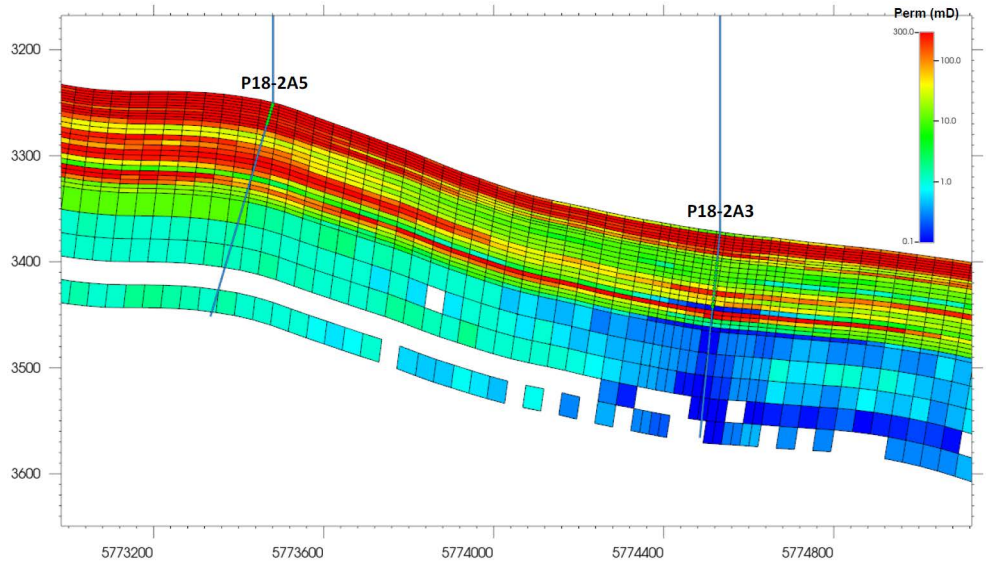

Figure 19—Permeability in the cross-section for P18-2A3 and P18-2A5 wells.

Table 3—Effective permeability × thickness (*kh*) comparison in the injection wells in P18-2 field.

Well	Effective permeability × thickness (mD-m)		
	P18-2A1	P18-2A3	P18-2A5
Hardegsen	120	21,730	8,530
Detfurth	40	3,535	4,380
Volpriehausen	2	3	65

In the P18-2A3 well, the "Base" injection scenario has been used (Figure 20) to show the effect of high permeability. The average rate is 1.5 × 10^6 sm^3/d (in P18-2A1, it is 1.7 × 10^6 sm^3/d) and the total CO2 injection volume is 7.2 × 10^9 sm^3 (14 million tons, and it is 13 million tons in P18-2A1). The injection temperature is 60-80°C except for the last year, when the injection temperature decreases to 40°C with higher rate of 1.7 × 10^6 sm^3/d. Thus overall the total CO2 volume in the P18-A3 well is comparable to the P18-2A1 well. The temperature distribution at the end of injection around the P18-2A3 well is shown in Figure 21. Compared to the P18-2A1 well (shown in Figure 13), the cold CO2 zone around P18-2A3 extends not only in the Hardegsen but also into the Detfurth zone. Moreover, the cold front is much less elongated as there is no fracture propagation during most of the injection. The significantly higher *kh* in the Detfurth in the P18-2A3 well (3,535 mD-m) than in the P18-2A1 well (40 mD-m) leads to an extensively distributed CO2 cold front in both the Hardegsen and Detfurth zones in P18-2A3 well. Figure 22 shows the evolution of the minimum effective stress in two locations: one in the Hardegsen and the other in the Detfurth and both locations show the lowest minimum effective stress during injection. It is important to note that the thermal fracturing conditions are solely achieved within the final year of injection, when the temperature of injection reaches 40°C due to much distributed CO2 cold front.

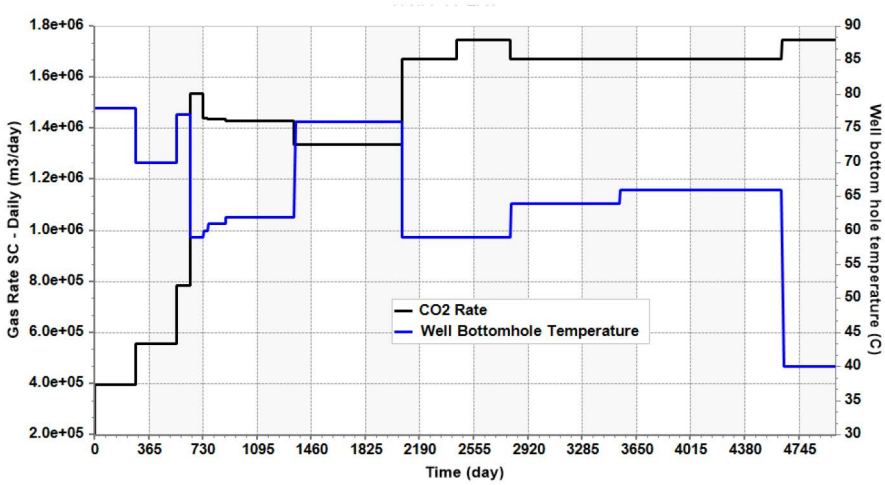

Figure 20—The base case injection scenario in P18-2A3 well.

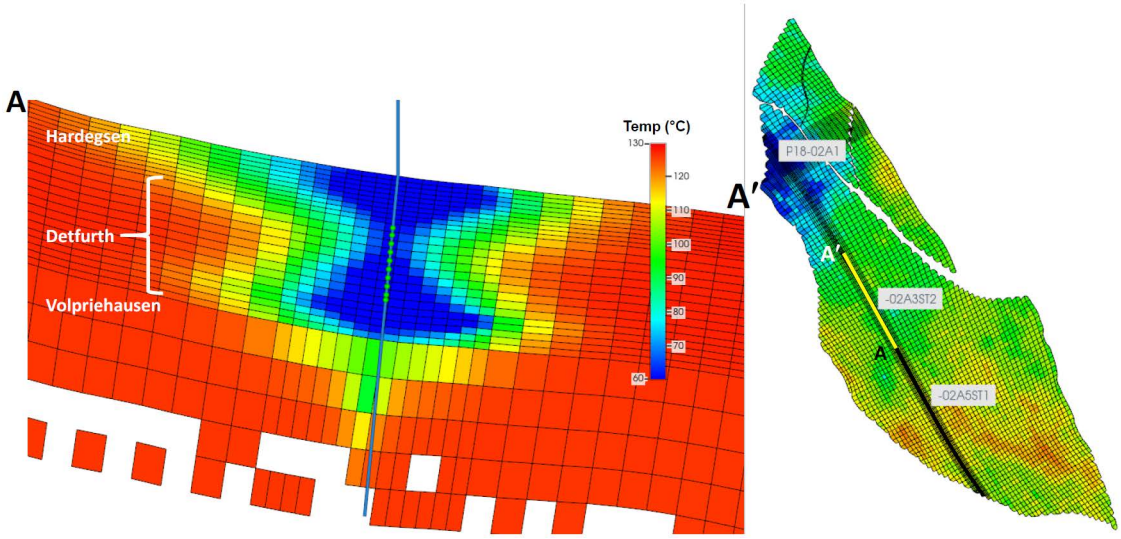

Figure 21—Temperature at the end of injection near the P18-2A3 well.

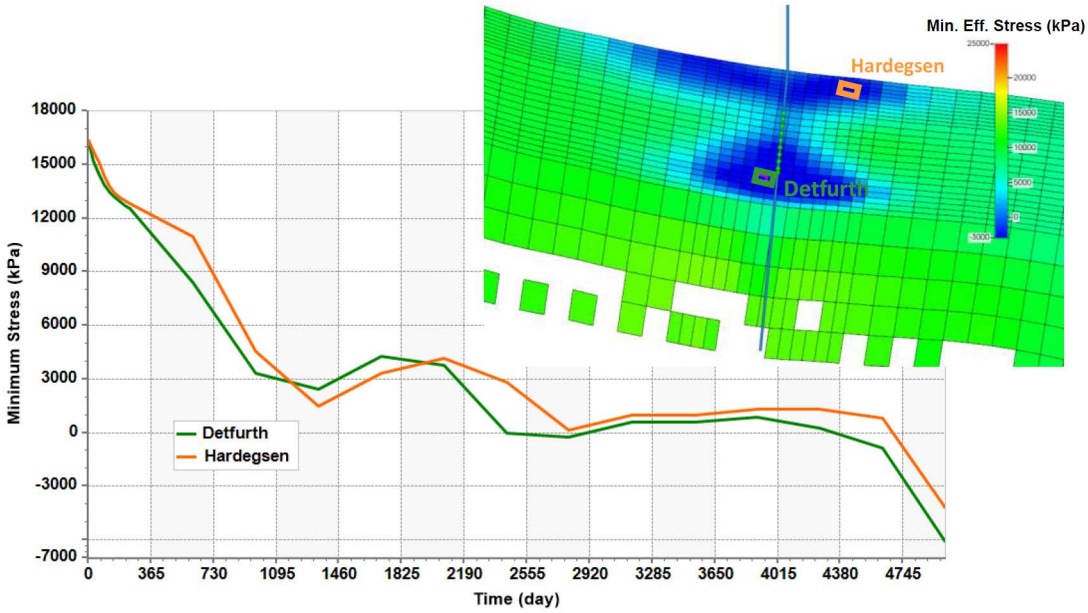

Figure 22—Minimum stress change in two cells: one in the Hardegsen and the other in the Detfurth formations.

Conclusions

- Thermal fracture propagation by CO2 injection into the depleted Dutch offshore gas field, P18, has been simulated by using coupled simulation. The model was populated with geomechanical properties and stresses obtained from log, from core tests, log analysis and leak-off-test and minifrac data. The principal parameters that determine the fracture propagation are stress, thermal expansion coefficient, modulus and permeability.
- Compared to matrix injection, the reduction of injection bottomhole pressure by thermal fracturing is 26,000 kPa for the worst injection scenario in P18-2A1 well. Therefore it is crucial to consider the potential implications of thermal fracturing when addressing flow assurance.
- Due to stress reduction by severe cooling the thermal fracture might propagate to the near-by fault in P18-2A1 well, which is located the closest to the near-by fault. This changes the temperature distributions at the boundary faults compared to matrix flow. These effects have to be included in the geomechanical fault stability analysis.
- Possibility for thermal fracturing propagation highly depends on the magnitude and variation of the permeability over the depth. If the permeability is high and much more equally distributed over its vertical extent (like for the P18-2A3 well) excess injection pressure will be modest and the penetration of the cold front may be limited, making it less plausible for a thermal fracture to propagate.

Reference

Arts, R. J.et al 2012. The feasibility of CO2 storage in the depleted P18-4 gas field offshore the Netherlands (the ROAD project). *International Journal of Greenhouse Gas Control* Volume **11** (Supplement) S10–S20 https://doi.org/10.1016/j.ijggc.2012.09.010

CMG. 2022. *GEM 2022.10 User Guide: Compositional & Unconventional Simulator*. https://www.cmgl.ca/gem

Crusen, M. C. M. 2018. Near wellbore effects induced by CO2 injection and the influence on injectivity in depleted gas reservoir. MSc Thesis, *TU Delft*, Delft, Netherlands (May 2018).

de Pater, C. J., Berentsen, C., and Park, J. 2021. P18 CCS: Seismic Risk Evaluation, *Delft*, The Netherlands: Fenix Consulting Delft B.V.

Fjær, E.et al 2008. *Petroleum Related Rock Mechanics 2nd Edition*. Amsterdam, The Netherlands: Elsevier

Neele, F., Wildenborg, T.et al 2019. CO2 storage feasibility in the P18-6 depleted gas field, *Utrecht*, The Netherlands: TNO.

Nordbotten, J. M. and Celia, M. A. 2012. *Geological Storage of CO2: Modeling Approaches for Large-Scale Simulation*. New Jersey, USA: John Wiley & Sons, Inc.

Porthos Partners. 2023. https://www.porthosco2.nl/en/project/